Detecting Goldstone modes with entanglement entropy

Bohdan Kulchytskyy,[1,*] C. M. Herdman,[1,2,3] Stephen Inglis,[4] and Roger G. Melko[1,5]
[1]*Department of Physics and Astronomy, University of Waterloo, Ontario N2L 3G1, Canada*
[2]*Department of Chemistry, University of Waterloo, Waterloo, Ontario N2L 3G1, Canada*
[3]*Institute for Quantum Computing, Waterloo, Ontario N2L 2Y5, Canada*
[4]*Department of Physics, Arnold Sommerfeld Center for Theoretical Physics and Center for NanoScience, University of Munich, Theresienstrasse 37, 80333 Munich, Germany*
[5]*Perimeter Institute for Theoretical Physics, Waterloo, Ontario N2L 2Y5, Canada*
(Received 15 February 2015; published 25 September 2015)

In the face of mounting numerical evidence, Metlitski and Grover (arXiv:1112.5166) have given compelling analytical arguments that systems with spontaneous broken continuous symmetry contain a subleading contribution to the entanglement entropy that diverges logarithmically with system size. They predict that the coefficient of this log is a universal quantity that depends on the number of Goldstone modes. In this paper, we confirm the presence of this log term through quantum Monte Carlo calculations of the second Rényi entropy on the spin-1/2 XY model. Devising an algorithm to facilitate convergence of entropy data at extremely low temperatures, we demonstrate that the single Goldstone mode in the ground state can be identified through the coefficient of the log term. Furthermore, our simulation accuracy allows us to obtain an additional *geometric* constant additive to the Rényi entropy, that matches a predicted fully universal form obtained from a free bosonic field theory with no adjustable parameters.

DOI: 10.1103/PhysRevB.92.115146 PACS number(s): 05.30.−d, 02.70.Ss, 03.75.Gg, 67.10.Fj

I. INTRODUCTION

In condensed matter, the entanglement entropy of a bipartition contains an incredible amount of information about the correlations in a system. In spatial dimensions $d \geqslant 2$, quantum spins or bosons display an entanglement entropy that, to leading order, scales as the boundary of the bipartition [1–3]. Subleading to this "area law" are various constants and—particularly in gapless phases—functions that depend nontrivially on length and energy scales. Some of these subleading terms are known to act as informatic "order parameters" which can detect nontrivial correlations, such as the topological entanglement entropy in a gapped spin-liquid phase [4–7]. At a quantum critical point, subleading terms contain novel quantities that identify the universality class, and potentially can provide constraints on renormalization-group flows to other nearby fixed points [8–15].

In systems with a continuous broken symmetry, evidence is mounting that the entanglement entropy between two subsystems with a smooth spatial bipartition contains a term, subleading to the area law, that diverges logarithmically with the subsystem size. First observed in spin-wave [16] and finite-size lattice numerics [17,18], the apparently anomalous logarithm had no rigorous explanation until 2011, when Metlitski and Grover developed a comprehensive theory [19]. They argued that, for a finite-size subsystem with length scale L, the term is a manifestation of the two long-wavelength energy scales corresponding to the spin-wave gap, and the "tower of states" arising from the restoration of symmetry in a finite volume [20–23]. Remarkably, their theory not only explains the subleading logarithm, but predicts that the coefficient is directly proportional to the number of Goldstone modes in the ground state. Furthermore, describing a Goldstone mode with a free scalar field theory allows them to predict the value for an additional additive *geometric* constant, which is fully universal and should therefore be the same across a wide range of continuum theories and lattice models.

In this paper, we confirm these predictions through large-scale quantum Monte Carlo (QMC) simulations on a spin-1/2 XY model on the square lattice. By employing an extended-ensemble generalization of a *ratio method* [24–26], we are able to carefully converge the mutual information of the second Rényi entropy to its low-temperature value. There, finite-size scaling reveals the coefficient of the subleading logarithmic term to precisely match the prediction of Metlitski and Grover, identifying the lone Goldstone mode in the theory. Remarkably, our simulations are accurate enough to also measure the universal additive geometric constant, which is consistent with the predicted relationship to the constant which appears in a lattice-regularized free scalar field theory [19].

II. ENTANGLEMENT ENTROPY IN THE TOWER OF STATES

To obtain a qualitative understanding of the origin of the logarithmic correction in Metlitski and Grover's theory, it is simplest to first envision decoupling the two spatial subsystems, A and B, that define the entangled bipartition. The low-energy degrees of freedom in each subsystem can be described by an $O(N)$ rotor ($N = 2$ for the XY model), representing the direction of the order parameter. Here we are only allowing global fluctuations of the order parameter within each subsystem, such that we may approximate the state of A and B each as a single independent quantum rotor. The effective Hamiltonian of each subsystem is

$$H = \mathbf{L}^2/2I,$$

where $\mathbf{L}^2$ is the total angular momentum operator with eigenvalues $\ell(\ell+1)$ and I is the effective moment of inertia

*Corresponding author: bohdan.kul@gmail.com

which is extensive, proportional to the magnetic susceptibility χ: $I \sim \chi L^d$ in d spatial dimensions [27]. Thus the energy scale of the tower $\Delta_{\rm tow} = 1/\chi L^d$ vanishes with the system volume, faster than any other energy scale. The eigenstates of $\mathbf{L}^2$ result in the famous "tower of states" observed routinely in computational studies of systems with continuous symmetry breaking in a finite volume [21–23].

The interaction between A and B which aligns the subsystem order parameters may be introduced via a Goldstone mode Hamiltonian H_G which couples the two rotors. The energy scale of the H_G is the Goldstone mode gap Δ_G which is the scale of the lowest energy spin waves. Since $\Delta_G \sim c/L$ where c is the spin-wave velocity, $\Delta_G \gg \Delta_{\rm tow}$ in the thermodynamic limit for $d > 1$. In the limit $\Delta_G \to \infty$, there are no *relative* fluctuations in the order parameter between subsystems, and A and B act as a single rigid rotor. For finite Δ_G, there will be relative fluctuations between the subsystems order parameters due to the zero-point fluctuations of H_G.

To estimate the entanglement entropy contribution from the tower of states, we can count the number of "accessible" states of subsystem A,Ω_A, when the total system is in the ground state, and use

$$S_{\rm tow} \sim \ln\Omega_A. \tag{1}$$

In the limit $\Delta_G \to \infty$ with the rotors rigidly coupled, the ground state is the ground state of the total system tower of states with zero total angular momentum: $\ell_{\rm AB} = 0$. In this case all states in the A subsystem tower are accessible to the ground state, as each state in A can be paired with an appropriate state in B to form a state with nonzero overlap with the $\ell_{\rm AB} = 0$ state. However, as discussed above, by including a *finite* Δ_G and thus allowing *relative* fluctuations of the subsystem order parameter between A and B, the fluctuations in the subsystem angular momentum are finite and determined by the ratio of the energy scales [19]:

$$\left\langle \mathbf{L}_A^2 \right\rangle \sim \Delta_G/\Delta_{\rm tow}.$$

In fact, the reduced matrix of the subsystem takes the form of a thermal density matrix with an effective "entanglement Hamiltonian" given by $H_{\rm tow}$ and the "entanglement temperature" given by Δ_G [19]; the resulting tower of states structure in the entanglement spectrum has been seen in numerics [28,29]. Thus the inclusion of Goldstone modes cuts off the accessible states of the subsystem to those with an energy below the spin-wave gap, as illustrated in Fig. 1.

As an example of this mechanism, consider the case of $N = 2$ (valid for our XY model simulations below). Here the rotors have a single component of angular momentum ℓ^z and the orientation of the rotors is described by a single angle θ. For $\Delta_G \to \infty$ the ground state has $\ell^z_{\rm AB} = 0$, which has nonzero overlap with states of equal and opposite ℓ^z in each subsystem: $|\ell^z_A = \ell, \ell^z_B = -\ell\rangle$; consequently all $|\ell^z_A\rangle$ state are accessible in this limit. We may include the effect of the lowest Goldstone mode by treating the dynamics of the relative angle between subsystems θ_δ as a single harmonic oscillator with frequency Δ_G and moment inertia $I_\delta \sim \Delta_{\rm tow}^{-1}$, with an effective

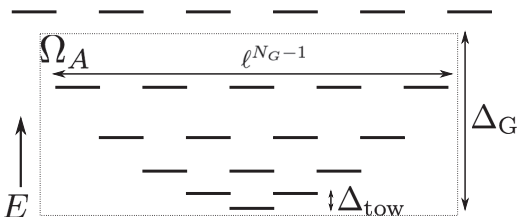

FIG. 1. Schematic energy-level structure of the low-energy tower of states for finite-size systems with spontaneous breaking of a continuous symmetry. The correction to the entanglement entropy may be approximated by the log of the number of quantum rotor states below the Goldstone gap Ω_A, which is represented by the states within the dotted box.

Hamiltonian

$$H_G = \frac{1}{2I_\delta} L_\delta^2 + \frac{1}{2} I_\delta \Delta_G^2 \theta_\delta^2. \tag{2}$$

Here, the fluctuations in the relative angular momentum L_δ are given by the ground state fluctuations of a harmonic oscillator:

$$\left\langle L_\delta^2 \right\rangle \sim I_\delta \Delta_{\rm G}/2 \sim \Delta_{\rm G}/\Delta_{\rm tow}.$$

The key point here is that because the order parameter is canonically conjugate to the rotor angular momentum, *increasing* the relative fluctuations in the order parameter *reduces* the fluctuations in L^2. Thus, allowing relative fluctuations of the order parameter between subsystems effectively cuts off subsystem rotor states that are accessed in the ground state at order $\ell \sim (\Delta_G/\Delta_{\rm tow})^{1/2}$—a relationship that holds for all N [19].

We may therefore estimate Ω_A by counting the number of states (in A's tower of states) that lie below Δ_G. For systems with $O(N)$ symmetry, the tower of states is described by a rotor living on an $N_G = N - 1$ dimensional sphere, where N_G is the number of Goldstone modes. The degeneracy of each energy level is of order ℓ^{N_G-1}. We then may estimate the total number of states below Δ_G by integrating the degeneracy up to the cutoff $\ell_{\rm co} = (\Delta_G/\Delta_{\rm tow})^{1/2}$:

$$\Omega_A \sim \int_0^{\ell_{\rm co}} d\ell \ell^{N_G-1} \sim \left(\frac{\Delta_G}{\Delta_{\rm tow}}\right)^{N_G/2}. \tag{3}$$

Using the relation $\chi = \rho_s/c^2$ from hydrodynamic spin-wave theory where ρ_s is the stiffness [30], the entanglement entropy correction due to the tower of states becomes

$$S_{\rm tow} \sim \frac{N_G}{2} \ln\left(\frac{\rho_s}{c} L^{d-1}\right). \tag{4}$$

We see that the logarithmic correction to the area law arises due to the quasidegeneracy of accessible bulk subsystem states, that scales as a power law in L for systems with spontaneously broken continuous symmetries. This contrasts with the leading-order area law, arising from the exponential scaling of the number of local boundary states with the boundary area. Clearly, the prefactor of the logarithmic correction is a universal number that simply counts the number of Goldstone modes.

III. QUANTUM MONTE CARLO PROCEDURE

In order to examine the effects of broken continuous symmetry on entanglement, we implement a highly efficient stochastic series expansion (SSE) QMC algorithm [31–33] for the two-dimensional (2D) spin-1/2 XY model,

$$H = J \sum_{\langle ij \rangle} \left(S_i^x S_i^x + S_i^y S_i^y \right).$$

This model is known to realize a ground state where the U(1) symmetry is spontaneously broken, resulting in one Goldstone mode. The finite-temperature SSE algorithm uses a version of the directed-loop update specialized to the XY model [34]. To measure the entanglement entropy, we employ a replicated simulation cell $Z[A,2,T]$, which gives access to a second Rényi entropy,

$$S_n = \frac{1}{1-n} \ln \left[\mathrm{Tr} \rho_A^n \right], \tag{5}$$

with $n = 2$. This is done through the ratio

$$\mathrm{Tr} \rho_A^2 = \frac{Z[A,2,T]}{Z[A=0,2,T]}, \tag{6}$$

where $Z[A=0,2,T] = Z[T]^2$, the square of the unmodified partition function [35]. One therefore needs to evaluate a difference in free energies or, alternatively, a ratio of partition functions, between the replicated and unmodified simulation cells with QMC. Several options are available, such as thermodynamic integration [35] and Wang-Landau sampling [36]. Alternatively, methods such as the *ratio method* [24–26] allow one to compute the partition function ratio directly. As described in the next section, for this model, careful convergence to low temperature is required. Hence, in Appendix A, we develop a highly efficient variant of the ratio method, dubbed the *extended ensemble ratio method*, applicable to a wide range of spin systems, and implemented specifically for the spin-1/2 XY model.

IV. RESULTS

We perform large-scale calculations to obtain the second Rényi entropy of the XY model on $L \times L$ square lattices with periodic boundary conditions. The resulting torus is partitioned into two cylindrical regions of linear dimension $L \times L_x^A$ and $L \times (L - L_x^A)$. For system sizes $L = 8,12,16$, separate finite-temperature tests are performed to explore the convergence of S_2. In agreement with the expected scaling of the tower-of-states gap, those results confirm that the convergence temperature scales approximately as $1/L^2$. We use this to estimate the convergence temperatures for $L = 20,24,28,32$.

Since SSE QMC simulations necessarily run at finite temperature, very small thermal contributions to S_2 are expected, which we observe to significantly affect our finite-size scaling analysis below. Fortunately, this thermal contribution can be essentially eliminated by employing the mutual information [35],

$$I_2(A:B) = S_2(A) + S_2(B) - S_2(AB).$$

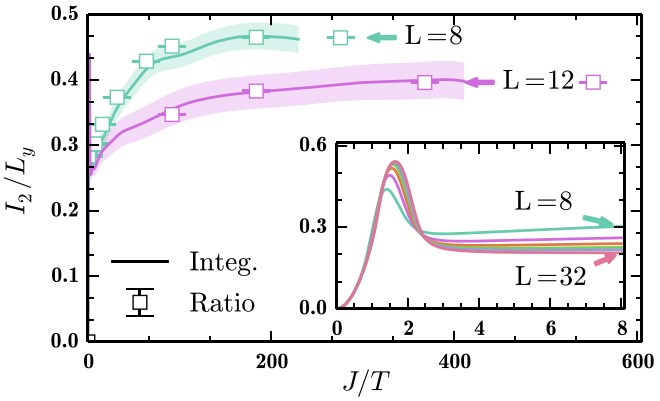

FIG. 2. (Color online) The mutual information of the $S = 1/2$ XY model as a function of $\beta \equiv J/T$. Solid lines are obtained through thermodynamic integration from $\beta = 0$, with statistical errors estimated by the shading. Square points with error bars are data obtained at a fixed β using the extended ensemble ratio method, described in Appendix A.

Assuming that bulk (volume-law) contributions from the two subsystems A and B approximately cancel the bulk term $S_2(AB)$ in I_2, the scaling form described by Metlitski and Grover becomes

$$I_2 = aL + N_G \ln \left(\frac{\rho_s}{c} L \right) + 2\gamma_{\mathrm{ord}}. \tag{7}$$

Here, a is a nonuniversal constant, ρ_s and c are the spin-wave stiffness and velocity, and γ_{ord} is the geometric constant that depends on the aspect ratios of the cylinders A and B [19]. Note, since nonuniversal (cutoff) dependencies are all contained within ρ_s and c, this geometric constant remains fully universal. For the spin-1/2 XY model on the square lattice, $\rho_s = 0.269\,74(5)J$ and $c = 1.1347(2)J$ were obtained from Ref. [37].

Figure 2 illustrates a representative convergence test for different system sizes. The mutual information peaks at temperatures above the Kosterlitz-Thouless transition of $(T/J)_{\mathrm{KT}} = 0.343$ (which can be detected by the crossing of the finite-size curves; see Ref. [38]). For $T/J < (T/J)_{\mathrm{KT}}$, the mutual information reaches a minimum (at $J/T \equiv \beta \approx 4$ in Fig. 2) before undergoing a slow rise. This rise continues until the approximate ground state is reached, for temperature below the finite-size scaling gap, which for system sizes larger than $L = 8$ occurs for $\beta > 100$. Thus, although the method of thermodynamic integration is useful to produce the general shape of the I_2 curve for a wide range of temperatures, it is difficult to control the systematic error introduced by numerical integration at low temperatures for $L > 12$. Therefore, data used in the below fits were converged at very low temperatures using the extended ensemble ratio method, described in Appendix A.

Figure 3 illustrates the resulting temperature-converged mutual information for a variety of system sizes, as a function of the "width" of the cylindrical region, L_x^A. Since, for a subsystem A and its complement B, $S_A = S_B$ only at $T = 0$, the symmetry of the entanglement entropy about $L_x^A/L = 1/2$ provides a sensitive test of temperature convergence. Employment of the "bare" Rényi entropy results in a very

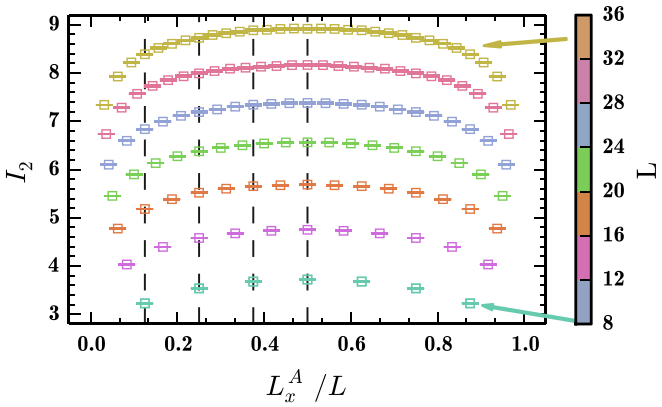

FIG. 3. (Color online) The mutual information as a function of torus aspect ratio, for the lowest temperatures examined for each system size. The corresponding β are 184, 368, 736, 1150, 1650, 2300, 3200, ordered from the smallest to the largest system size. Vertical dashed lines are the aspect ratio values employed in the fitting in Fig. 4.

slight asymmetry in the curve; use of I_2 restores these symmetry producing high-quality data that can be fitted using Eq. (7).

The results of this analysis are illustrated in Fig. 4. Here, I_2 is calculated at various aspect ratios [the vertical cuts in Fig. 3 and fit to the functional form Eq. (7)]. Specifically, to extract the coefficient of the subleading logarithm, the mutual

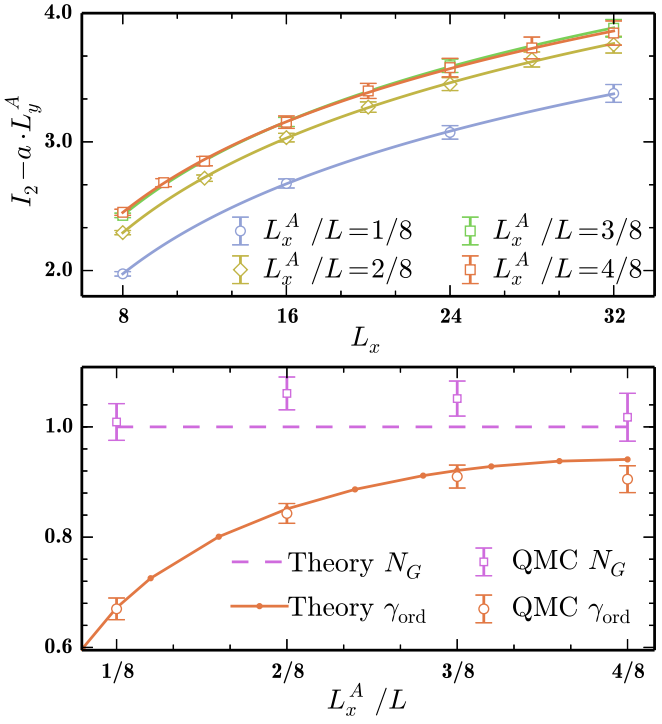

FIG. 4. (Color online) The top figure displays a three-parameter fit to the functional form $aL + b\ln(L\rho_s/c) + d$ for different torus aspect ratios, where b gives a value for $N_{\rm G}$. Another three-parameter fit to $aL + \ln(L\rho_s/c) + 2\gamma_{\rm ord} + d/L$ (not shown) is employed to extract the geometrical constant $\gamma_{\rm ord}$. The resulting $N_{\rm G}$ and $\gamma_{\rm ord}$ are shown alongside the theoretically predicted values at bottom.

information was fit to

$$I_2 = aL + b\ln\left(\frac{\rho_s}{c}L\right) + d,$$

where a, b, and d are adjustable fit parameters. As illustrated in Fig. 4(a), there is definitive evidence for the existence of a logarithm; furthermore, independent fits for the four aspect ratios studied each give $N_{\rm G} = 1$ to within error bars. We note that additional $1/L$ corrections have no significant effect on the extracted value of N_G, but inclusion of a $1/L$ term requires fixing d to the theoretical value, since accurate four-parameter fits are not possible with this data set (see Appendix B).

Even more striking, we are able to extract the universal shape dependence of the geometric constant $\gamma_{\rm ord}$. Since $1/L$ corrections pollute the constant term, to extract $\gamma_{\rm ord}$ we assume the theoretical value of $N_G = 1$ and perform fits to the functional form

$$I_2 = aL + \ln\left(\frac{\rho_s}{c}L\right) + 2\gamma_{\rm ord} + \frac{d}{L}.$$

Thus calculated, $\gamma_{\rm ord}$ for $N = 2$ in two dimensions can be compared via a zero-parameter fit to the subleading constant term $\gamma_{\rm free}$ calculated in a free scalar field theory [19] through the relation

$$\gamma_{\rm ord} = \gamma_{\rm free} + \tfrac{1}{2}\ln(2\pi),$$

valid for the second Rényi entropy. The free field result $\gamma_{\rm free}$, which depends on the aspect ratio L_x^A/L, can be calculated numerically for free bosons on the lattice using the correlation matrix technique (as in Ref. [39]). As illustrated in Fig. 4(b), the resulting theoretical curve is in excellent agreement with our QMC results for $\gamma_{\rm ord}$.

V. DISCUSSION

In this paper, we have employed large-scale quantum Monte Carlo (QMC) simulations on the spin-1/2 XY model to demonstrate the presence of a logarithmic correction to the Rényi entropy due to spontaneous breaking of continuous symmetry. This term arises from the presence of two infrared energy scales in the problem: the spin-wave gap, and the "tower of states." The coefficient of this logarithm is predicted in Ref. [19] to be $N_{\rm G}(d-1)/2$, where $N_{\rm G}$ is the number of Goldstone modes and d the spatial dimension. We confirm this prediction through finite-size scaling studies on the square lattice XY model, recovering to high precision the expected $N_{\rm G} = 1$. In order to do so, a QMC algorithm was developed to sample the second Rényi entropy at a fixed temperature with high efficiency (described in Appendix A).

In addition to confirming $N_{\rm G} = 1$, our technique is able to converge the value of an additive geometric constant $\gamma_{\rm ord}$, which is fully universal and has a functional dependence on the geometric aspect ratio of the entangled bipartition. This function matches, to within error bars, that calculated using a free scalar field theory regularized on a toroidal square lattice, with no adjustable parameters [19].

Finally, armed with the *a posteriori* knowledge of Eq. (4), one can revisit the analysis of QMC data for the Heisenberg model [17,18]. Based on a similar analysis as that presented here, we conclude that the Heisenberg model data of Ref. [17] contains a much weaker "signal-to-noise" ratio than the XY model. Indeed, for the Heisenberg model, the coefficient of the area law, as well as the coefficient of the $1/L$ correction, are more than an order of magnitude larger than the corresponding coefficients for the XY model. At the same time, the signal from the logarithmic and constant terms are comparable (or smaller) to those in the XY model. Hence, although the Heisenberg data of Ref. [17] are consistent with the prediction of Ref. [19], it is difficult to obtain conclusive agreement with unconstrained fits on small system sizes.

In conclusion, our work on the XY model is a rare example of quantitative agreement between a universal quantity calculated in continuum field theory and finite-size lattice simulations. The ability of the Rényi entanglement entropy to mediate between continuum theory and lattice simulation illustrates the utility of such geometric quantities as a complementary approach to study correlations in condensed-matter systems. In this case, with the full understanding of the universal structure of the entanglement entropy in the presence of a spontaneously broken continuous symmetry, the door is now open to the examination of Goldstone modes in a large variety of systems, through the calculation of Rényi entropies.

ACKNOWLEDGMENTS

We are thankful for enlightening discussions with A. Läuchli, D. Poilblanc, K. Resch, and particularly, M. Metlitski and T. Grover, without whom this work would not have been possible. Support was provided by Natural Sciences and Engineering Research Council of Canada, the Canada Research Chair program, and the Perimeter Institute (PI) for Theoretical Physics. Research at PI was supported by the Government of Canada through Industry Canada and by the Province of Ontario through the Ministry of Research & Innovation. S.I. acknowledges support from FP7/ERC Starting Grant No. 306897. The simulations were performed on the computing facilities of SHARCNET.

APPENDIX A: EXTENDED-ENSEMBLE RATIO METHOD

1. Preliminaries

In this section, we describe a quantum Monte Carlo (QMC) algorithm for estimating the Rényi entropy [defined in Eq. (5)], using an extended-ensemble version of the so-called "ratio method" that was applied in this context by Humeniuk and Roscilde [25]. In the present work, the algorithm will be specialized to the case of the second Rényi entropy ($n = 2$), although extensions to other n are relatively straightforward. Similarly, although we concentrate on applications to the spin-1/2 XY model, generalizations to Hamiltonians with other symmetries are possible (see subsection A 4 below).

QMC estimators for the second Rényi entropy S_2 rely on the fact that the trace over powers of the reduced density matrix can be related to a ratio of partition functions as given in Eq. (6) where the numerator is the partition function of a multisheeted Riemann surface [35,40] (a "replicated" QMC simulation cell), and the denominator is the square of the regular partition function. In the replicated case, the geometry of the entangled region A dictates the "boundaries" of the $d+1$-dimensional QMC simulation cell; world lines in region A are periodic in imaginary time with period 2β (or $n\beta$), while in region B, two (or n) independent replicas exist with periodicity β.

Since the logarithm in Eq. (5) reduces the calculation of S_2 to the difference in free energies between systems described by the two partition functions, thermodynamic integration or Wang-Landau techniques can be used to devise QMC estimators. In contrast, *ratio methods* (not to be confused with the related "ratio trick" coined in Ref. [41]) give an estimator for the ratio of partition functions, and act as valuable alternatives to explicit calculation of free energies. The most distinct advantage of ratio methods is their ability to calculate S_n directly at a given fixed temperature. They can however be inefficient for large entropies (large subregions A), and may require several separate simulations of different subregion geometries (that can be combined with the ratio trick) to combat this.

2. Algorithm for the XY model

We begin by generalizing Eq. (6) to the problem of calculation the ratio of replicated partition functions defined with two arbitrary regions A and A'; namely $Z[A',2,T]/Z[A,2,T]$. As with all ratio methods, the QMC estimator in this case is based on a simple identity [24]:

$$\frac{Z_{A'}}{Z_A} = \left\langle \frac{W_{A'}(c)}{W_A(c)} \right\rangle_A , \tag{A1}$$

where we have simplified our previous notation $Z_A = Z[A,2,T]$. The expectation value is taken in the Z_A ensemble and $W_{A'}(c)$ and $W_A(c)$ are the weights of a configuration c in the $Z_{A'}$ and Z_A ensembles, respectively.

The difficulty of applying this identity in a straightforward manner is that it is valid only when the configuration space of $Z_{A'},\Omega_{A'}$, is contained within the configuration space of Z_A,Ω_A—that is $W(c) \neq 0$ for any c. Unfortunately, this condition is not automatically satisfied when the standard labelling variables are used in conventional QMC techniques. However, for the XY model, by introducing a new label, it is possible to recast the configuration spaces of both ensembles such that $\Omega_A = \Omega_{A'}$. In other words, a common label c can be found that enumerates all possible configurations within both ensembles. This label can be formally linked to an updating procedure in the well-known loop algorithm [42]. Within this framework, nonlocal changes of configuration space are achieved through so-called loop variables, defined on top of the original configuration space. In this context, our algorithm can be viewed as an "improved estimator."

Here we will consider a stochastic series expansion (SSE) representation of the partition function [31–33]. A term in the SSE expansion of Z can be represented by a spin state and an operator list, where the operators are terms in the Hamiltonian. Alternatively, we can represent the same configuration by a linked list of vertices [34]; an example of a set of vertices is displayed in Fig. 5. We can therefore label the configuration by the list of links l and the set of vertex types $v^A(l)$ for a given boundary condition defined by A as shown in Fig. 6. Here we

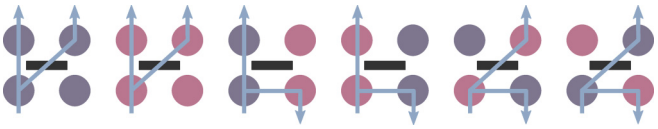

FIG. 5. (Color online) The six types of vertices present in a SSE simulation of the XY model [34]. The colored circles represent two possible states of a spin 1/2. The horizontal solid bar depicts a two-site operator. The lines with arrow tips show all possible nonbounce moves for a given vertex when the entrance leg is the left-most bottom one. There are two of those moves for each vertex.

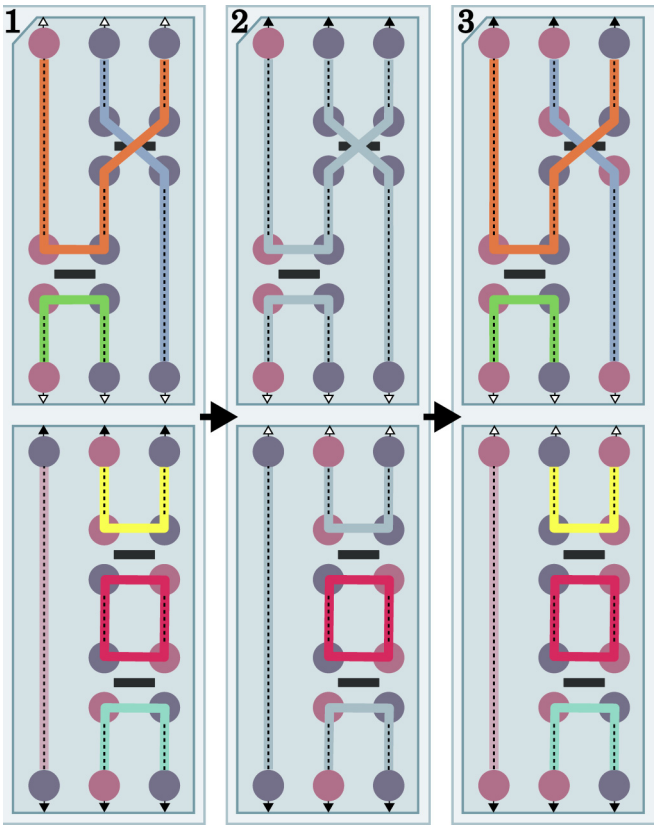

FIG. 6. (Color online) A three-step conversion process of a vertex configuration $v^A(l)$ into $v^{A'}(l)$ that preserves its segment partition. The details of this process are illustrated in the text. At each step, a simulation cell composed of two replicas (top and bottom) is shown. The dashed vertical lines between adjacent legs that are located on different vertices form a linked list. The label l identifies different sets of those lines. The two types of small arrows placed next to the replicas' boundary slices mark the boundary conditions along the dimension of the expansion: within a column, spins decorated with the same kind of arrows are connected. In this way, the first simulation cell's region A is empty while the other two simulation cells' region A' contains all three spins. Open colored solid lines trace out a segment partition of the first and third simulation cells (seven segments total). Note that within the same cells, there is also a single closed segment, an inner loop, composed of four legs. In the second simulation cell, the open segments are merged by boundary connections to form a single cross-replica loop identified by the same color. Mismatching boundary spins along this loop are flipped according to the algorithm presented in the text, resulting in a vertex configuration compatible with the new boundary conditions as displayed in the third simulation cell.

have defined l to include all "internal" links between vertices and we link the "exterior" vertices to the boundaries of the operator string; we specifically do not close the links at the boundaries, as one would do in a regular $d+1$-dimensional QMC simulation cell [34].

These two labels are sufficient to identify the configuration space of many models. Thus, a partition function can be expressed as the following double sum:

$$Z_A = \sum_{l} \sum_{v^A(l)} W[v^A(l)], \tag{A2}$$

where $W[v^A(l)]$ is the weight of a configuration labeled by l and $v^A(l)$.

This general expression can be simplified for the XY model. The model's SSE vertices are displayed in Fig. 5. With an appropriate choice of adjustable SSE constants, the weight of each vertex becomes equal to $1/2J$ [34]. Hence, the weight of a vertex configuration does not depend on a particular combination of vertices in the list and, therefore, is completely defined by the length of the corresponding operator list alone. We get that $W_{XY}[v^A(l)] = W_{XY}(l)$ and Eq. (A2) is simplified to

$$Z_A^{XY} = \sum_{l} W_{XY}(l) \sum_{v^A(l)} 1. \tag{A3}$$

The second sum counts the degeneracy of vertex configurations compatible with the boundary conditions between replicas. Motivated by the search for a variable independent of those boundary conditions, we introduce a new label, $s[v^A(l)]$, that enumerates all possible partitions of a vertex configuration labeled by $[l, v^A(l)]$ into a set of nonoverlapping segments. The following algorithm is used to construct a single instance of those segments:

(1) Pick an unmarked leg located on a boundary slice. Mark it as visited.

(2) By following the linked list, switch to a leg connected to it.

(3) The new leg belongs to a vertex.

(i) If this vertex is unmarked, pick with an equal probability one of two possible nonbounce moves for this vertex and switch to the corresponding leg. Mark this vertex as visited and store the move type.

(ii) If the vertex is marked, switch to the next leg by performing a move of the same type that was done before.

(4) Repeat steps 2–4 until a leg on a boundary slice is reached.

By repeating this algorithm for all legs located on the boundary slices, all open segments are traced out. However, it is possible that some of the legs located on the inner slices have been left unmarked after this procedure. In order to partition those remaining legs too, the closed segments (loops) need to be traced. This is achieved by adjusting two steps of the algorithm. Now in the first step, the choice of legs to be picked is extended to all interior legs. Once the initial leg is picked, the algorithm proceeds in the same way until it reaches the same leg again. Hence, the condition to terminate the execution of the fourth step has to be modified appropriately. By construction, any two segments built in such a manner can never pass through the same leg and, therefore, are nonintersecting.

The loop tracing continues until all legs are marked. By the end of this procedure every leg belongs to one single segment (closed or open). This constitutes a single instance of the partitioning of a vertex configuration into a set of nonoverlapping segments. An example of such a partition is shown in the first cell of Fig. 6. Note that at each vertex, there are two choices for how to proceed with the construction of a segment. Each of them leads to a different partition.[1] Therefore, a simulation cell that contains N_v vertices can be partitioned in 2^{N_v} distinct ways. This is the range of the newly introduced label s. Since N_v just counts the number of vertices without discerning their types, the number of partitions for a particular $v^A(l)$ is determined by the l label only. This fact allows us to rewrite Eq. (A3) in a new form:

$$Z_A^{XY} = \sum_l \frac{W_{XY}(l)}{2^{N_v(l)}} \sum_{v^A(l)} \sum_{s[v^A(l)]} 1. \tag{A4}$$

This expression is obtained from Eq. (A3) by introducing a third sum via the substitution $1 = \frac{1}{2^{N_v(l)}} \sum_{s[v^A(l)]} 1$ where the new sum is performed over all different partitions of $v^A(l)$.

It can be also shown that for any vertex configuration in $A, v^A(l)$, partitioned as $s[v^A(l)]$, there exists a vertex configuration in $A', v'^{A'}(l)$, with exactly the same partitioning, that is $s[v'^{A'}(l)] = s[v^A(l)]$. The proof is by construction. If $v^A(l)$ and $v'^{A'}(l)$ were the same, the task is trivial. Otherwise, $v^A(l)$ has to be modified in order to satisfy the boundary conditions of A'. An example of such a process is displayed in Fig. 6. Here, the first and third simulation cells represent $v^A(l)$ and $v'^{A'}(l)$ correspondingly. The second cell depicts an intermediate step of the correctional procedure. Here, the open segments are connected into a loop along which the boundary spin mismatches are fixed one by one. Further details of the algorithm are given below.

Proceeding column by column, consider each pair of boundary legs, (s_1^0, s_2^0), to be matched with respect to the new boundary conditions A'. If the legs align, $s_1^0 = s_2^0$, proceed to the next pair. Otherwise, randomly choose one of the two legs in the pair. Say it is s_1^0. Since this leg is located on a boundary slice, it belongs to an open segment. Flip all legs belonging to this segment. Now, the original pair of legs is properly aligned, however there might be another mismatch at the other end of the segment. Call the new pair (s_1^1, s_2^1) where s_2^1 is the leg that has just been flipped as part of the open segment. By the same logic as before, s_1^1 must belong to an open segment whose other end is identified as another boundary leg s_2^2. If $s_1^1 \neq s_2^1$, flip this segment in order to align the (s_1^1, s_2^1) pair and move on to the next pair (s_2^2, s_1^2). Otherwise, proceed to the same pair without flipping the segment. In this way, one by one pairs of boundary legs are aligned with respect to A' boundary condition along a loop of open segments. An important subtlety occurs at the last step of this algorithm when the last pair (s_2^n, s_2^0) is considered. Unlike previously, s_2^1 cannot be flipped if those legs do not align. An attempt to do so would entail another iteration of corrections with the same result, thus, initiating the algorithm in an infinite loop.

However, this does not occur in the XY model due to the special properties of its vertices. Notice that the only vertex move that connects two antialigned legs is the "switch-and-reverse" move (Fig. 5); this is the only move that reverses the vertical directionality of propagation of the segment's head. Consequently, once a segment tracing is initiated with the choice of a leg and its state, the spin state of the leg at the segment's head is determined by the vertical direction that the segment passes through the leg. On the last boundary connection, the direction of motion along the segment must be the same as the initial direction, and therefore the initial spin state at the head of the segment under construction is always the same as its final state. We see then that for any segment partition of $v^A(l)$, it is always possible to construct a $v'^{A'}(l)$ with the same segment partition.

Now that we have shown the equivalence between any two configuration spaces constraint by boundary conditions A and A' in terms of the segment partitions, we have achieved our initial goal to find a label s that can be used to apply Eq. (A1). However, we still need to compute the weights of $W^A(s)$ and $W^{A'}(s)$. Upon a close inspection of the inner double sum in Eq. (A4), we realize that the same segment partitions can be generated from different vertex configurations. This degeneracy can be exploited in order to replace the double sum with a single sum:

$$Z_A^{XY} = \sum_l \frac{W_{XY}(l)}{2^{N_v(l)}} \sum_{s(l)} \deg^A[s(l)], \tag{A5}$$

where the inner sum iterates over all unique segment partitions for a given linked list and $\deg^A[s(l)]$ is the degeneracy of the segment partition labeled as $s(l)$. As will be shown, the degeneracy depends on the boundary conditions between replicas and, thus, the superscript must be included.

In order to calculate the degeneracy of a segment partition $s(l)$, connect open segments using boundary conditions A to form $N_b^A[s(l)]$ loops that cross boundary slices. In addition to those loops, there are also $N_i[s(l)]$ inner loops (closed segments). Since all those loops do not intersect with each other by construction, the spins within them can be flipped independently. Each combination of the loops' flips leads to another vertex configuration. Equivalently, all of those vertex configurations generate the same segment partition $s(l)$. There are in total $N_b^A[s(l)] + N[s(l)]$ loops with each one being in one of two states: flipped or not flipped. Each combination of those states corresponds to a different vertex configuration. In total, there are $2^{N_b^A[s(l)]+N_i[s(l)]}$ of such combinations which constitutes the degeneracy $\deg^A[s(l)]$.

With the last piece of the puzzle in our hands, we infer the segment partition weight from Eq. (A5):

$$W_{XY}^A[s(l)] = \frac{W_{XY}(l)}{2^{N_v(l)}} 2^{N_b^A[s(l)]+N_i[s(l)]}. \tag{A6}$$

Since the inner loops are unaffected by the boundary conditions, upon the substitution of this weight in Eq. (A1) their number drops out and an elegant expression is

[1]Two partitions are considered equal when all their segments are the same. In its turn, for two segments to be considered the same, the order of legs in the construction of one segment must match exactly with the order of legs in the construction of another segment.

obtained:

$$\frac{Z^{XY}_{A'}}{Z^{XY}_{A}} = \langle 2^{N_b^{A'}[s(l)]-N_b^{A}[s(l)]} \rangle_A. \tag{A7}$$

In practice, this estimator can be implemented in fewer steps that were required to prove its validity. It requires two routines. One routine traces out a random single segment partition $s(l)$ for a vertex configuration $v^A(l)$ as was outlined before. In order to speed up the execution, it is not necessary to identify the closed segments. The end product of this routine is to associate the pairs of boundary spins that are connected via open segments. Once this step is done, the second routine takes the set of those pairs together with replicas' boundary conditions as its inputs. Its task is to count N_b^A. This routine is executed for both A and A' with the same open segments. In the end, $N_b^{A'}[s(l)]$ and $N_b^{A}[s(l)]$ are known and the estimator can be evaluated according to Eq. (A7).

3. Benchmarks

To illustrate the efficiency of the new estimator, its raw measurements are compared to the original ratio method [25] in Fig. 7 of the 2D XY model of interest in the main text. The deterioration of the two estimators can be seen as the difference in region sizes, $\Delta A = A' - A$, becomes large. As the reference values, we employ the results obtained from the ratio trick [41], which constitute a compilation of the extended ensemble (EE) ratio method results from many different Monte Carlo simulations, each executed with $\Delta A = 1$. Note that the original ratio method results are based on five times more Monte Carlo sweeps than were involved to produce the EE ratio method results. Even with such advantage, the ratio method statistics become increasingly poor towards $\Delta A = 22$. After this threshold, the estimator seems no longer capable to capture any meaningful statistics within the running time of its simulations. The performance of the EE is strikingly better. Even when $\Delta A = 64$, the largest possible increment

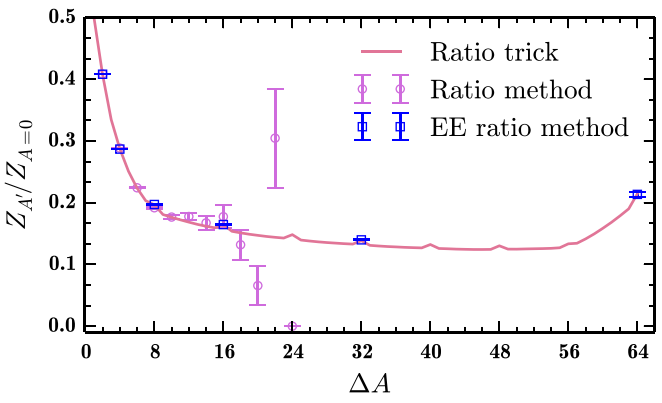

FIG. 7. (Color online) The comparison of ratio methods efficiencies in an 8×8 system with periodic boundary conditions at $\beta = 8$. The ratio of partition functions measurement is plotted against the size difference between their corresponding regions A, ΔA. The ratio method completely fails for $\Delta A > 22$, and thus the data are not shown on the plot. The values obtained from the ratio trick serve as a reference. The statistical error in those values is contained within the width of the curve.

in the system, it produces an accurate result with a precision comparable to the ratio method precision at $\Delta A = 10$.

4. Extensions to other models

Although the previous discussion has focused specifically on the XY model, the framework of the extended ensemble ratio trick can be applied in a more general context. In order to understand the more general procedure, let us trace through the steps in the derivation of Eq. (A7) where the unique properties of the XY model are used. The first such step is done in the very beginning: in going from Eq. (A2) to Eq. (A3), it is assumed that all SSE vertices have equal weights. For other models with different symmetries, we can identify two classes: those with equal weights, and those without.

For other models with equal-weight vertices, the extension of the algorithm is straightforward. Essentially, the relevant model weights simply replace the specific XY weights, W_{XY}. For models with imaginary-time loop updates, like the spin-1/2 Heisenberg model, Eq. (A7) remains fully valid with the same procedure of counting the number of boundary loops, N_b^A. One expects that all SU(N)-invariant models (with general N) will have this same form of highly efficient estimator, which should facilitate the accurate estimation of Rényi entropies in these cases. More generally, in equal-weight models with other imaginary-time structures, such as branching clusters in the case of the transverse-field Ising model [43,44], these loop counters will simply be replaced by the numbers of analogous branching clusters. Thus, we expect the extended ensemble ratio trick to straightforwardly produce an efficiency gain in a wide variety of important models.

The second class of models is the case of reduced symmetry, where the assumption of equal vertex weights is no longer valid. To incorporate this generalization in the derivation, we avoid the specialization to the XY model by skipping Eq. (A3). The derivation from this point on continues without change until Eq. (A4) which is modified to

$$Z_A = \sum_l \frac{1}{2^{N_v(l)}} \sum_{v^A(l)} W[v^A(l)] \sum_{s[v^A(l)]} 1, \tag{A8}$$

where we simply moved the vertex weight inside the second sum.

The discussion following this equation is concerned with showing the independence of the partition label $s[v^A(l)]$ on boundary conditions A. Let us stress that as long as this property holds for a model in question, the framework of the extended ensemble ratio trick applies. In general, the proof of this property is achieved through the demonstration that for any segment partition of a vertex configuration $v^A(l)$, there exists a configuration $v'^{A'}(l)$ with exactly the same partition. For the XY model, the key point in the proof revolves around the properties of the vertex set displayed in Fig. 5. Namely, it is the property that the only move that switches the leg color is the one that changes the vertical directionality of propagation as well. Let us note that due to this feature, the whole argument is oblivious to the type of lattice the Hamiltonian is defined on, thus, making the estimator Eq. (A7) applicable to models on lattices beyond the bipartite one considered in the study. Furthermore, the above-mentioned set of vertices is not

limited to the XY model. Indeed, it is common to all XXZ models (including the Heisenberg model) in a magnetic field or without it. Alternatively, for a different class of models defined on a different set of vertices, it is possible to construct an argument not relying on the aforementioned feature of the XXZ vertices. However, it is most likely to depend on the underlying lattice. For instance, on a bipartite lattice the fact that an even number of lateral moves is required to get back to the same spin can be used for vertex sets in which the only moves that change the leg color are the ones that move onto the neighboring spins ("switch" moves).

Assuming that the existence of a common label $s[v^A(l)]$ independent of the boundary conditions can be proven, it is always possible to switch the order of the two inner sums in Eq. (A8) such that the two outer sums iterate over the same configuration space of segment partitions:

$$Z_A = \sum_l \frac{1}{2^{N_v(l)}} \sum_{s(l)} \sum_{v^A[s(l)]} W\{v^A[s(l)]\}. \tag{A9}$$

As before, Eq. (A9) is used to extract the weight of a segment configuration. This time however, the vertices in the most inner sum have unequal contributions to the weight of a given partition. Since it is the only difference, the argument following Eq. (A5) can be reused, thus leading to a new expression for the weight of a segment partition:

$$W^A[s(l)] = \frac{1}{2^{N_v(l)}} \sum_{v^A[s(l)]} W\{v^A[s(l)]\}. \tag{A10}$$

This sum iterates over $2^{N_b^A[s(l)]+N_i[s(l)]}$ different vertex configurations compatible with boundary conditions defined by region A.

Last, we substitute this weight into Eq. (A1) to obtain a generalized version of the estimator Eq. (A7):

$$\frac{Z_{A'}}{Z_A} = \left\langle \frac{\sum_{v^{A'}[s(l)]} W^{A'}\{v^{A'}[s(l)]\}}{\sum_{v^A[s(l)]} W^A\{v^A[s(l)]\}} \right\rangle_A. \tag{A11}$$

Note that Eq. (A7) can be recovered from this expression for any model with the vertex weights independent on a particular vertex configuration, that is $W\{v^A[s(l)]\} = W(l)$. For instance, this is the case for the Heisenberg model.

In practice, the cost of a straightforward evaluation of this estimator is likely to overcome the gains associated with dramatically improved statistics observed for the XY model (Fig. 7). This consideration is based on two complications that were not present in the simplified version, Eq. (A7). First of all, instead of just counting the number of closed loops compatible with the given boundary conditions, it is now necessary to iterate through all vertex configurations generated by flipping all combinations of those loops in order to calculate the sum in Eq. (A11). Second, unlike in the case for models with equal vertex weights for which only open segments are required to be traced out, in a more general case the inner segments need to be identified as well. Furthermore, those segments can also be used to generate vertex configurations as mentioned in the previous point. Since the number of vertex configurations is exponential in the number of the inner segments, it is expected that the performance of the generalized estimator is prohibitively dependent on the simulation temperature. Further studies are required to determine the stringency of those complications and whether they can be overcome in a general case.

APPENDIX B: DATA AND FITS

In order to extract the coefficients of interest, we subject our mutual information measurements to a thorough fitting analysis (see Tables I and II). We start by establishing the consistency of the data with the scaling behavior of Eq. (4) from the main text. This is achieved via fits 1 and 3 where the logarithmic coefficient as well as the geometric constant are set to the predicted values. By comparing the χ_k^2 of those fits, we note the importance of the finite-size correction a_4/L. We then proceed with a four-parameter fit (fit 6) in an attempt to simultaneously extract both coefficients of interest. However, a dramatic increase in the error bars of the extracted values signals an overfitting, caused by a limited range of available system sizes. Instead, three-parameter fits (4 and 5) with the a_4/L term included are performed by setting either a_2 or a_3 to their respective putative values; these fits provide values in an excellent agreement with the theory [19]. We also note from three-parameter fit 2 that disregarding the a_4/L term has a much larger negative effect on the extracted values of a_3 than on the values of a_2. Such effect is consistent with a stronger relative contribution from the logarithmic term to the total value of the mutual information, as compared to that from the constant term. Thus we conclude that with this data set, we can extract the log coefficient without any assumptions about the theoretical values of the coefficients, since fit 2 (with no theoretical assumptions or $1/L$ correction) results in a_2 values that are consistent with those extracted from fit 5 (which includes a $1/L$ correction at the cost of assuming the theoretical value of a_3). However, to accurately extract the geometric constant from these data, we must include a $1/L$ correction term and thus fix a_2 to its theoretical value.

TABLE I. Mutual information values I_2 used in Fig. 4 from the main text.

	L							
L_x^A/L	8	10	12	16	20	24	28	32
1/8	3.227(3)			5.183(7)		6.83(1)		8.39(1)
2/8	3.538(5)		4.583(7)	5.52(1)	6.379(9)	7.18(2)	7.99(2)	8.73(2)
3/8	3.679(6)			5.66(1)		7.34(2)		8.89(2)
4/8	3.720(6)	4.27(1)	4.75(1)	5.69(1)	6.56(1)	7.38(2)	8.17(3)	8.92(2)

TABLE II. Fitting coefficients, labeled as a_i, extracted from Table I with the help of various functional forms. The last column shows the χ^2 per degree of freedom that can be used as a measure of the goodness of fit. γ_{ord} refers to the theoretical value of the geometric constant which is aspect ratio dependent. The expected theoretical value [19] for a_2 is 1, while for a_3 they are 0.672, 0.851, 0.921, 0.941 as arranged in the order from the smallest to the largest aspect ratio correspondingly.

Fit no.	Fitting function	L_x^A/L	a_1	a_2	a_3	a_4	χ_k^2
1	$a_1 L + \ln(L\rho_s/c_{sw}) + 2\gamma_{ord}$	1/8	0.1561(4)				3.7
		2/8	0.155(1)				23.0
		3/8	0.155(2)				26.0
		4/8	0.155(1)				11.0
2	$a_1 L + a_2 \ln(L\rho_s/c_{sw}) + 2a_3$	1/8	0.157(2)	1.01(3)	0.663(4)		0.85
		2/8	0.155(2)	1.06(3)	0.806(4)		0.67
		3/8	0.156(2)	1.05(3)	0.876(3)		0.27
		4/8	0.158(3)	1.02(4)	0.899(6)		0.73
3	$a_1 L + \ln(L\rho_s/c_{sw}) + 2\gamma_{ord} + a_4/L$	1/8	0.1567(2)			−0.10(2)	0.42
		2/8	0.1569(2)			−0.51(4)	0.64
		3/8	0.1572(2)			−0.51(3)	0.2
		4/8	0.1570(4)			−0.52(6)	0.89
4	$a_1 L + \ln(L\rho_s/c_{sw}) + 2a_3 + a_4/L$	1/8	0.157(1)		0.67(2)	−0.1(2)	0.82
		2/8	0.157(1)		0.84(2)	−0.4(2)	0.76
		3/8	0.158(1)		0.91(2)	−0.4(3)	0.32
		4/8	0.159(2)		0.91(2)	−0.1(3)	0.75
5	$a_1 L + a_2 \ln(L\rho_s/c_{sw}) + 2\gamma_{ord} + a_4/L$	1/8	0.157(2)	1.00(3)		−0.10(4)	0.81
		2/8	0.158(2)	0.99(3)		−0.50(5)	0.78
		3/8	0.158(2)	0.99(3)		−0.49(4)	0.33
		4/8	0.161(3)	0.95(4)		−0.47(7)	0.82
6	$a_1 L + a_2 \ln(L\rho_s/c_{sw}) + 2a_3 + a_4/L$	2/8	0.145(8)	1.4(3)	0.6(2)	3.0(2)	0.57
		4/8	0.140(9)	1.6(3)	0.5(2)	4.0(2)	0.44

[1] L. Bombelli, R. K. Koul, J. Lee, and R. D. Sorkin, Phys. Rev. D **34**, 373 (1986).
[2] M. Srednicki, Phys. Rev. Lett. **71**, 666 (1993).
[3] J. Eisert, M. Cramer, and M. B. Plenio, Rev. Mod. Phys. **82**, 277 (2010).
[4] A. Hamma, R. Ionicioiu, and P. Zanardi, Phys. Lett. A **337**, 22 (2005).
[5] A. Hamma, R. Ionicioiu, and P. Zanardi, Phys. Rev. A **71**, 022315 (2005).
[6] A. Kitaev and J. Preskill, Phys. Rev. Lett. **96**, 110404 (2006).
[7] M. Levin and X.-G. Wen, Phys. Rev. Lett. **96**, 110405 (2006).
[8] E. Fradkin and J. E. Moore, Phys. Rev. Lett. **97**, 050404 (2006).
[9] H. Casini and M. Huerta, Nucl. Phys. B **764**, 183 (2007).
[10] R. C. Myers and A. Singh, J. High Energy Phys. 09 (2012) 013.
[11] R. R. P. Singh, R. G. Melko, and J. Oitmaa, Phys. Rev. B **86**, 075106 (2012).
[12] S. Inglis and R. G. Melko, New J. Phys. **15**, 073048 (2013).
[13] A. B. Kallin, K. Hyatt, R. R. P. Singh, and R. G. Melko, Phys. Rev. Lett. **110**, 135702 (2013).
[14] J. Helmes and S. Wessel, Phys. Rev. B **92**, 125120 (2015).
[15] T. Grover, Phys. Rev. Lett. **112**, 151601 (2014).
[16] H. F. Song, N. Laflorencie, S. Rachel, and K. Le Hur, Phys. Rev. B **83**, 224410 (2011).
[17] A. B. Kallin, M. B. Hastings, R. G. Melko, and R. R. P. Singh, Phys. Rev. B **84**, 165134 (2011).
[18] J. Helmes and S. Wessel, Phys. Rev. B **89**, 245120 (2014).
[19] M. A. Metlitski and T. Grover, arXiv:1112.5166.
[20] P. W. Anderson, Phys. Rev. **86**, 694 (1952).
[21] B. Bernu, C. Lhuillier, and L. Pierre, Phys. Rev. Lett. **69**, 2590 (1992).
[22] C. Lhuillier, arXiv:cond-mat/0502464.
[23] G. Misguich and P. Sindzingre, J. Phys.: Condens. Matter **19**, 145202 (2007).
[24] A. Gelman and X. -L. Meng, Stat. Sci. **13**, 163 (1998).
[25] S. Humeniuk and T. Roscilde, Phys. Rev. B **86**, 235116 (2012).
[26] D. J. Luitz, X. Plat, N. Laflorencie, and F. Alet, Phys. Rev. B **90**, 125105 (2014).
[27] A. W. Sandvik, in *Lectures on the Physics of Strongly Correlated Systems XIV: Fourteenth Training Course in the Physics of Strongly Correlated Systems*, edited by A. Avella and F. Mancini AIP Conf. Proc. No. 1297 (AIP, Melville, NY, 2010), p. 135.
[28] F. Kolley, S. Depenbrock, I. P. McCulloch, U. Schollwöck, and V. Alba, Phys. Rev. B **88**, 144426 (2013).
[29] V. Alba, M. Haque, and A. M. Läuchli, Phys. Rev. Lett. **110**, 260403 (2013).
[30] B. Halperin and P. Hohenberg, Phys. Rev. **188**, 898 (1969).
[31] A. W. Sandvik and J. Kurkijärvi, Phys. Rev. B **43**, 5950 (1991).
[32] A. W. Sandvik, J. Phys. A **25**, 3667 (1992).
[33] A. W. Sandvik, Phys. Rev. B **59**, R14157 (1999).
[34] O. F. Syljuåsen and A. W. Sandvik, Phys. Rev. E **66**, 046701 (2002).
[35] R. G. Melko, A. B. Kallin, and M. B. Hastings, Phys. Rev. B **82**, 100409 (2010).

[36] S. Inglis and R. G. Melko, Phys. Rev. E **87**, 013306 (2013).
[37] F.-J. Jiang, Phys. Rev. B **83**, 024419 (2011).
[38] J. Iaconis, S. Inglis, A. B. Kallin, and R. G. Melko, Phys. Rev. B **87**, 195134 (2013).
[39] I. Peschel and V. Eisler, J. Phys. A **42**, 504003 (2009).
[40] P. Calabrese and J. Cardy, J. Stat. Mech.: Theory Exp. (2004) P06002.
[41] M. B. Hastings, I. González, A. B. Kallin, and R. G. Melko, Phys. Rev. Lett. **104**, 157201 (2010).
[42] H. G. Evertz, Adv. Phys. **52**, 1 (2003).
[43] A. W. Sandvik, Phys. Rev. E **68**, 056701 (2003).
[44] R. G. Melko, in *Strongly Correlated Systems—Numerical Methods*, edited by A. Avella and F. Mancini (Springer, Berlin, 2013), pp. 185–206.